

N-body Simulations of Mergers based on Giant Radio Galaxy Fornax A

ELKO GERVILLE-REACHE,¹ JEFFREY KENNEY,¹ AND SHASHANK DATTATHRI¹

¹ Yale University Department of Astrophysics

ABSTRACT

The giant elliptical radio galaxy Fornax A is dominated by complex kinematics and an irregular molecular gas distribution indicating it experienced one or more violent galactic scale mergers in the past ~ 1 Gyr. Its proximity and brightness makes it an ideal candidate for understanding the complicated dynamics between stellar matter and gas in the context of galaxy mergers. In this thesis work, we ran a set of N-body galaxy merger simulations of collisionless stellar particles between a large Hernquist spherical galaxy and a smaller rotating disk. The simulation assumed a mass ratio of 10:1 between the galaxies and investigated the effects of collisions with high radial components and different disk inclinations.

Keywords: Galaxies (573) — Galaxy Interactions (608) — N-Body simulations (1082)

1. INTRODUCTION

Fornax A (NGC 1316) is a giant elliptical radio galaxy located in the outer edges of the Fornax galaxy cluster at a distance of 20.8 ± 0.5 Mpc. The brightest member of its cluster, Fornax A is also the third brightest nearby radio source at 259 Jy after Centaurus A (NGC 5128) and M87 (E. Iodice et al. 2017). NGC 1316 is characterized by complex morphological features with strong evidence pointing to a rich history of merger events. The galaxy has been studied extensively in optical and infrared wavelengths, revealing the complicated morphology that makes up NGC 1316. Two distinct components can be mapped, with the main galactic body consisting of a spheroid with dust and gas scattered throughout. This central spheroid contains highly irregular molecular gas (CO) clouds with high velocity dispersions and disrupted kinematics (Kenney, 2013). Numerous long, tidally compressed filaments and blobs are scattered radially throughout the core (see figure 2), strongly suggesting one or more recent mergers took place ~ 1 Gyr ago, and is evidence Fornax A is still in the process of relaxing (E. Iodice et al. 2017). At large radii $\sim 33 \leq R \leq 200$ kpc from the galaxy center, the galaxy consists of a vast stellar envelope with dust patches and elongated loops of stellar matter (E. Iodice et al. 2017). (F. Schweizer 1980) provided the first detailed account of Fornax A in literature, identifying loops L1-L5 surrounding the galactic nucleus of the galaxy, of which L5 dominates in size. A giant HII region was also detected south of the galactic center. Later using the ESO VST, E. Iodice et al. (2017) discovered numerous fainter

loops L6-L9 in the outer edges of the stellar envelope. These loops are likely tidally distorted, expelled stellar matter disrupted by a violent merger, and are still in the process of assembling into a relaxed state. Integrated g-r color analysis revealed a wide range of colors in the galaxy, with loops L2 and L3 notably being ~ 0.13 mag bluer than the average color of Fornax A, indicating possible external origin. From derived M/L ratios, E. Iodice et al. (2017) estimated a total mass of $5.2 \leq M \leq 8.3 \times 10^{11} M_{\odot}$. Being situated in the Fornax cluster, NGC 1316 is surrounded by other smaller galaxies, of which NGC 1317 appears very close in projection to NGC 1316. Yet due to the absence of tidal distortions in NGC 1317's disk, it is reasonable to assume they have not interacted strongly at this present time (Richtler, T. et al. 2014).

The CO gas distribution in the central region $r \sim 6$ kpc has a highly irregular spatial distribution and highly disturbed kinematics (Maccagni, F. M. et al. (2020), Kenney, J.D.P. (2025)). Many of the molecular clouds adjacent to each other have large differences in velocity, and in some regions, there are multiple clouds along the line of sight, with velocities differing by 100-500 km/s (see figure 1). These indicate that the molecular gas is not distributed in a thin rotating disk but rather has a non-planar configuration with clumps on irregular orbits. Kenney, J.D.P. (2025) propose this is largely due to the gas clumps from a disrupted accreted galaxy settling into the new gravitational potential. In support of this argument, 95% of the CO flux is located in 2 opposing quadrants, unlike a gas disk, but resembling

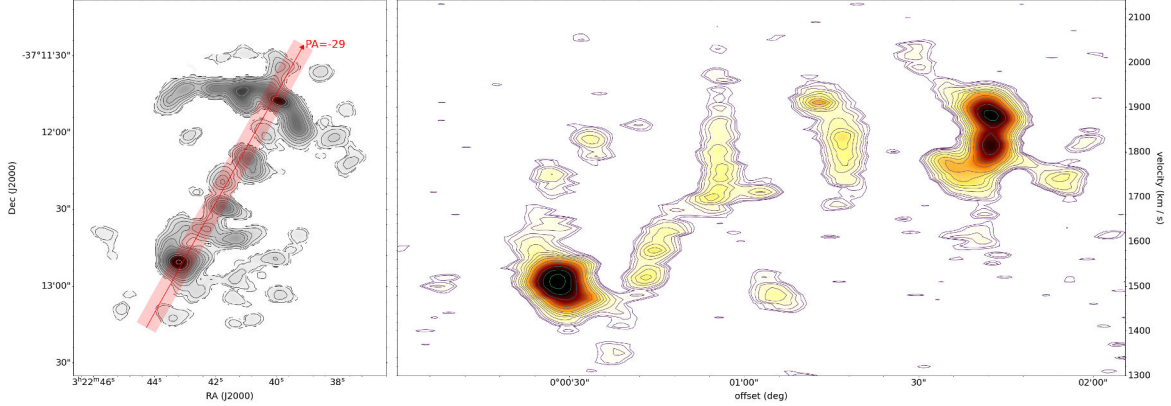


Figure 1. Left panel: Intensity plot of molecular CO gas found in the central core of NGC 1316, its distribution closely following the dust features visible in figure 2. The red line displays the main axis along the gas where the positions and velocities along the line of sight were measured. Right panel: Position v. line of sight velocity diagram corresponding to the gas along the red line. Figure adapted from Kenney, J.D.P. (2025).

merger debris from mergers with large radial components. Early-type galaxies such as Fornax A typically have little to no gas, further supporting that most of it came from in-fall during a violent merger. However, gas also experiences multiple non-gravitational forces, including frictional forces between the gas components of the 2 galaxies, and shocks and winds driven by radio jet outbursts. Collisions between the gas particles further average out random motions over time, creating complex kinematics. We wish to learn how much of the irregularities in the spatial distribution and kinematics of the molecular gas can be understood by gravitational effects alone during a merger, and how much is due to non-gravitational effects on the gas. Thus, we investigate simple galactic merger simulations consisting only of collisionless stellar particles to see which of the irregular CO features present in Fornax A might be caused solely by gravitational effects.

2. SETTING UP AND RUNNING N-BODY SIMULATIONS OF GALAXIES AND MERGERS

For this investigation, we ran a set of galactic merger simulations between a spheroidal early-type galaxy and a disk galaxy with a 10:1 mass ratio. This mass ratio is based on observed total gas mass estimates of $\sim 10^9 M_\odot$ in Fornax A and typical stellar to gas mass ratios in spiral galaxies, suggesting the perturber galaxy likely had a mass of $\sim 10^{10} M_\odot$ (L. Lanz et al. 2010). The early-type galaxy representing Fornax A was modeled from a Hernquist density profile, which benefits from having spherical symmetry and thus greatly simplifies calculations. Simple axisymmetric rotating disks of particles, on the other hand, are much harder to model in equilibrium and were generated using the Agama Python package (E. Vasiliev 2018). A total of three different simulation runs were modeled, with varying disk incli-

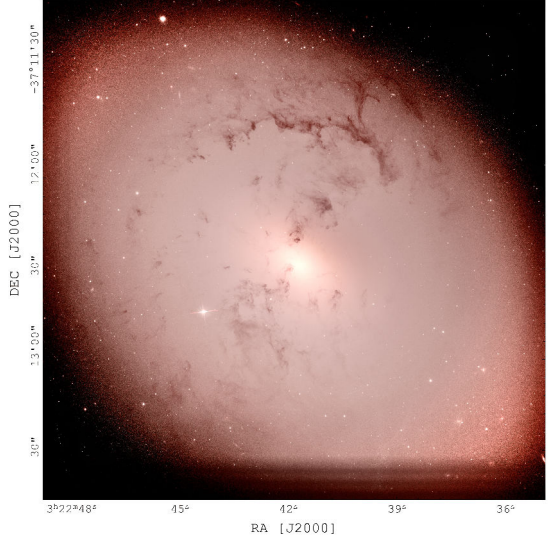


Figure 2. Logarithmic scaled HST image [F555W and F814W] of central 2' (10 kpc) of NGC 1316. The dust is strongly correlated with CO emission, and shows the disturbed state of the cold dense ISM. The image is of the same scaling as the left panel of figure 1. Data downloaded from proposal ID 9409.

nations and impact parameters, to try and understand how these might impact the molecular gas distribution in the merger remnant.

This thesis project focuses on understanding how to properly set up and run N-body simulations of galaxies and simulate mergers between them. The entire project and simulation analysis was written in Python, with the exception of the disk galaxy model code, adapted from (E. Vasiliev 2018). The following sections 2.1-2.5 describe the mathematical theory and code implementation of N-body simulations as well as the methods of generating self-gravitating N-body models for each galaxy.

The process of assessing a particular model's energetic stability in isolation before running a simulation is also discussed. Consequently, the majority of this work is on running N-body simulations rather than applying them to Fornax A, which would require more complex simulations.

2.1. The N-Body Problem

The N-body problem in astrophysics attempts to solve the motion of N bodies through space under their mutual gravitational attraction. For a system of $N = 2$ bodies, there exists an analytical solution to their trajectories, allowing accurate predictions of their positions and velocities at some future time t . The conical orbit sections and Kepler's laws are derived from this solution. The problem arises when $N \geq 3$, where the chaotic nature of the system does not result in a solvable analytical solution, as shown in figure 3. Chaotic systems are not random in nature, but instead are characterized by having a unique solution for every set of initial conditions. These systems are highly sensitive to changes in initial conditions, where seemingly small fluctuations can lead to highly divergent solutions. For small numbers of N , constraints can be made to approximate the trajectories accurately. However, when studying globular clusters or galaxies, $N \simeq 10^6 - 10^{11}$, therefore complicating calculations a great deal. This lack of an analytical solution warrants a numerical approach for predicting the orbits of systems with large N . Numerical approximations integrate the equations of motion of each particle in discrete timesteps Δt , recursively using the previous set of positions and velocities to compute the next timestep. Consequently, the accuracy of these calculations are highly dependent on the size of Δt as well as the number of timesteps, since integrating longer into the future will accumulate more numerical errors.

2.2. N-Body Code

In this simulation, all particles are assumed to be collisionless, baryonic, stellar masses. Extragalactic systems can be characterized by their relaxation time, which measures how long it takes for a star's trajectory to be significantly perturbed by the other stars. In a system of N particles, $t_{\text{relax}} \simeq \frac{N}{8 \ln N} t_{\text{cross}}$, with the crossing time defined as $t_{\text{cross}} = R/v$, or the average time it takes for a star to cross the system. For a typical galaxy with $N \simeq 10^{11}$ stars and $t_{\text{cross}} \simeq 10^8$ years, the relaxation time is much greater than a typical simulation timescale, allowing for collisions to be safely ignored. Galaxies are a few hundred crossing times old and therefore can be approximated as collisionless systems even during a violent merger event. In globular clusters, however, the

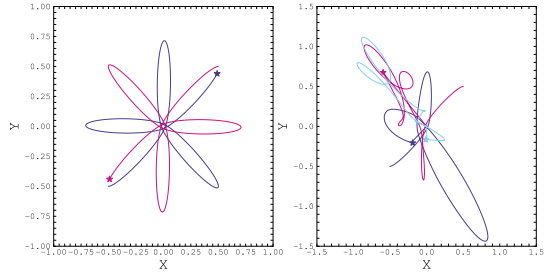


Figure 3. Left panel: N-body simulation of 2 equal mass stars producing a symmetrical, rosette-shaped orbit. Right panel: The exact same system perturbed by a third, equal mass companion. The chaotic nature arising from the third body is very apparent. Note the different axes scales.

crossing time and number of stars are much lower, so stellar encounters may be of importance over the lifetime of the cluster ([J. Binney & S. Tremaine 1987](#)). The simulations exclude the dark matter halo, central bulge, black hole, and gas particles, all of which are significant components of real galaxies. These approximations are necessary to keep N low enough to run the simulation on a personal computer, as well as ensure the system is collisionless. Gas particles are collisional by nature, and require more advanced techniques, such as fluid simulations, to properly simulate. The N-body code therefore assumes gravity as the only force operating on the particles. Given a set of particles with initial positions and velocities, the next timestep is computed by brute force using the leapfrog algorithm. For each particle, the gravitational acceleration acting onto it is obtained by summing the pairwise contributions from all other particles. Thus, the acceleration g_i on particle p_i can be expressed as a sum over all other particles j ,

$$g_i = G \sum_j^N \frac{m_j(r_j - r_i)}{(|r_j - r_i|^2 + \epsilon^2)^{3/2}}, \quad (1)$$

where r is the position vector in 3D space and ϵ is the gravitational softening length. ϵ ensures the effects of close encounters are smoothed, and that dividing by zero does not occur. Its value is determined by the number of particles based on a relation derived by [W. Dehnen \(2001\)](#) for Plummer spheres, given by

$$\epsilon = 0.017 \left(\frac{N}{10^5} \right)^{-0.23}, \quad (2)$$

and also serves as the simulation resolution. Close encounters between particles with a distance smaller than ϵ cannot be resolved. Once the acceleration is computed, the positions and velocities of the next timestep are calculated using the standard kinematic equations of motion. The leap-frog algorithm computes the velocities

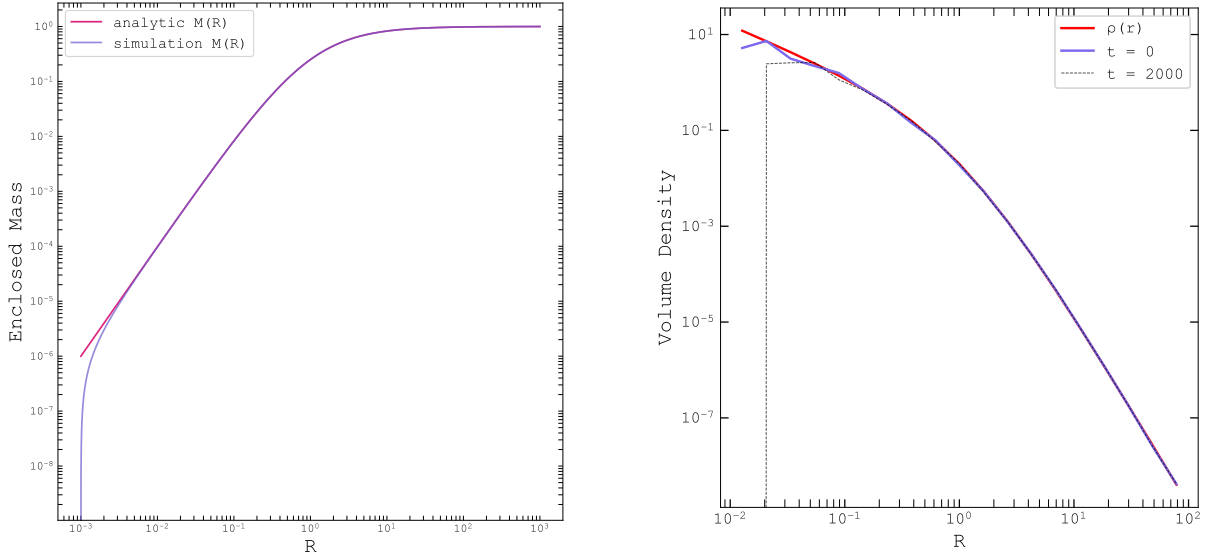


Figure 4. Left panel: Simulation enclosed mass distribution $M_{\text{enc}}(R)$ compared to the analytical enclosed mass distribution for a Hernquist sphere. Right panel: Density of the Hernquist model $\rho(r)$ at the start and end of the simulation run overplotted against the analytical distribution. At $t = 2,000$, the density drops off from the expected value at $R \simeq \epsilon$ which is to be expected since the softening length sets the simulation resolution.

and positions at interleaved timesteps, where the velocities are calculated at half timesteps before and after computing the new positions using the equations

$$v_{t+\frac{1}{2}} = v_t + g_t \frac{\Delta t}{2} \quad (3)$$

$$x_{t+1} = x_t + v_{t+\frac{1}{2}} \Delta t. \quad (4)$$

This creates a 'kick,' 'drift,' 'kick' method conserving energy with second order precision and is a good trade-off between accuracy and computational efficiency. The new positions are then used to calculate a new set of accelerations, continuing the cycle endlessly. The leap-frog method is also time reversible, making it a standard choice in most N-body codes.

Direct particle-particle summation may be the most accurate class of N-body simulations, but comes with a heavy computational price of $O(N^2)$ time, placing an upper limit on the number of particles in the simulation on the order of $\sim 10^5$. This was achieved by parallelizing the acceleration computation to leverage all cores of the computer, by decomposing the calculation into small blocks. Increasing the number of cores would undoubtedly allow more particles. The integrator saves the phase space coordinates x, y, z, v_x, v_y, v_z , and potential $\phi_i = \frac{1}{m_i} \sum_j \frac{G m_j}{|r_j - r_i + \epsilon|}$ of each particle every 10 timesteps as a $N \times 7$ matrix. Moreover, in all simulation runs, model units are assumed, where the gravitational constant G , the total system mass M , and scale length α are all set equal to 1. The models are then easily scaled relative to each other by multiplying the initial

phase space coordinates and masses by scalar quantities. Furthermore, in these models each particle represents a large collection of stars since the simulations in this investigation are of the order $N \propto 10^{4-5}$, or many orders of magnitude less than real galaxies. Certain features seen in merger remnants, such as stellar shells and loops, require large numbers of particles to resolve. As such, simulating millions of particles requires both heavy computational power from computer clusters and more efficient N-body integration schemes.

2.3. Generating Initial Conditions

In attempting to model NGC 1316, a spherical Hernquist density profile was chosen, notable for its spherical symmetry and analytic solution. The mass density is given by

$$\rho(r) = \frac{M\alpha}{2\pi r(r + \alpha)^3}, \quad (5)$$

where M represents the total mass of the system and α , the scale length or the radius at which the density starts to drop off. Integrating the mass density over r computes the enclosed mass within a radius R , given by

$$M_{\text{enc}}(R) = 4\pi \int_0^R r^2 \rho(r) dr. \quad (6)$$

Both distributions are shown in figure 4, overplotted against the analytical distributions for a Hernquist sphere. Ensuring that these distributions match is crucial to building stable galaxy models. Inverse transform sampling is then used to generate a set of radii that

follow the Hernquist density profile. Separating these radii into their 3-dimensional x, y, z initial positions is made simple by taking advantage of the profile's symmetry using spherical coordinates, giving the following relations

$$x = r \sin \theta \cos \phi \quad (7)$$

$$y = r \sin \theta \sin \phi \quad (8)$$

$$z = r \cos \theta. \quad (9)$$

Spherical symmetry allows for the azimuthal angle to be uniformly distributed in the range $\phi \in [0, 2\pi]$. The radial angle must be more carefully generated since uniformly generating θ would result in over-densities at the poles. Thus, $\theta = \arccos(x)$, where x is uniformly distributed over the interval $[-1, 1]$. For a system of N particles, N pairs of (ϕ, θ) angles are generated. Having generated a set of particles following the Hernquist distribution, their velocities must be computed next. When assigning velocities to each particle, great care must be taken to ensure that all are bound to the galaxy if the system is to be in equilibrium. For a Hernquist sphere, the number of stars at any given energy level is described by the distribution function (DF)

$$f(\mathcal{E}) = \frac{1}{\sqrt{8\pi^2}} \int_0^{\mathcal{E}} \frac{d^2\rho}{d\Psi^2} \frac{d\Psi}{\sqrt{\mathcal{E} - \Psi}}, \quad (10)$$

where \mathcal{E} and Ψ are the relative energy and relative potential given by $\mathcal{E} \equiv -E = \Psi - \frac{1}{2}v^2$ and $\Psi \equiv -\Phi$. The potential Φ is given by

$$\Phi = -\frac{GM}{r + \alpha}. \quad (11)$$

$f(\mathcal{E})$ is defined to be 0 for all $\mathcal{E} < 0$ and non-negative for $\mathcal{E} \geq 0$ (J. Binney & S. Tremaine 1987). This distribution is plotted in figure 6, left panel. In this paper, all energy and potential calculations follow relative convention. To compute the magnitude of the velocity for a given particle, it is critical that its magnitude is less than the escape velocity at that position, defined as $v_{esc} = \sqrt{2|\Psi|}$. It can be shown that the probability of a particle p_i having some velocity v is proportional to $v^2 f(\Psi_i - \frac{1}{2}v^2)$, where Ψ_i is the potential of the particle and v is some velocity in the range $[0, v_{esc}]$ (J. Binney & S. Tremaine 1987). Integrating this probability density function over v for each particle across its range of acceptable velocities generates a cumulative distribution function, which can be used to assign a velocity magnitude to each particle using inverse transform sampling. This method ensures each particle is bound to the system by only choosing velocities within the allowed energy levels. Similarly to the position components, the 3-dimensional v_x, v_y, v_z components of the

velocities are assigned using spherical coordinates. Having generated the initial phase space coordinates of our N-body model, the individual particle masses, m are initialized using the equation $m = \frac{M}{N}$, where M is the total galaxy mass and N the total number of particles. This assumes the total mass of the galaxy is distributed evenly across each particle. The galaxy generation function outputs a $N \times 7$ matrix file containing the positions, velocities, and masses of the galaxy.

2.4. Testing Initial Conditions

Once suitable initial conditions are generated, as demonstrated in figure 5, it is important to ensure the galaxy behaves as expected in isolation. Interactions between galaxies fundamentally alter the structure and energy of the galaxies, necessitating that the galaxy models stay in energetic equilibrium when simulated with no external forces present. The initial phase space coordinates and masses are loaded into Python arrays and fed into the N-body code, which also requires the number of timesteps and Δt as arguments. The softening length is automatically calculated based on the number of particles in the simulation. The N-body algorithm computes the positions, velocities, and potential of the particles for each timestep using the integration scheme described in section 2.2 and saves them as simulation snapshots. Once completed, the output files are loaded back into Python and run through the analysis pipeline. The total energy \mathcal{E} is computed from the velocities and potential, and plotting the histogram of this distribution shows the Number of particles at a given energy level, $N(E)$. We can also use the analytical model once again to verify the results of the simulation, given by the equation $N(E) = f(E)g(E)NdE$, where $g(E)$ is the density of states (J. Binney & S. Tremaine 1987). A galaxy in equilibrium should not deviate from the analytical curve after many timesteps of integration. Figure 6 (right panel) shows the normalized distribution of energies $N(E)$ for the start and end times of the simulation run. The distributions closely agree with the analytical model, with the curve corresponding to $t = 2,000$ only slightly deviating from the expected analytical values. This confirms that in isolation, the spherical galaxy model is in equilibrium.

2.5. Perturber Galaxy

The perturbator galaxy was modeled as a single component disk galaxy, without a dark matter halo or central bulge and black hole to keep N sufficiently low. The gas component inherent to spiral galaxies was also left out due to the collisionless constraint of our simulation. Initial conditions were generated with the

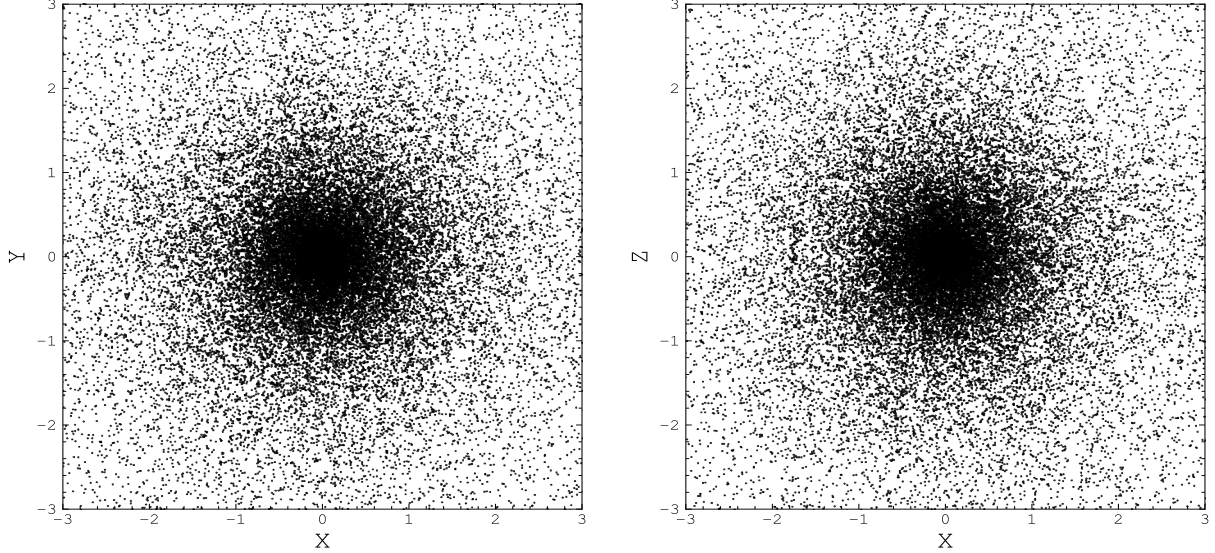


Figure 5. Various orthogonal projections of a Hernquist model initial positions with $N = 20,000$ particles, mass $M = 1$, and scale radius $\alpha = 1$. The galaxy's spherical symmetry is apparent across the different projections.

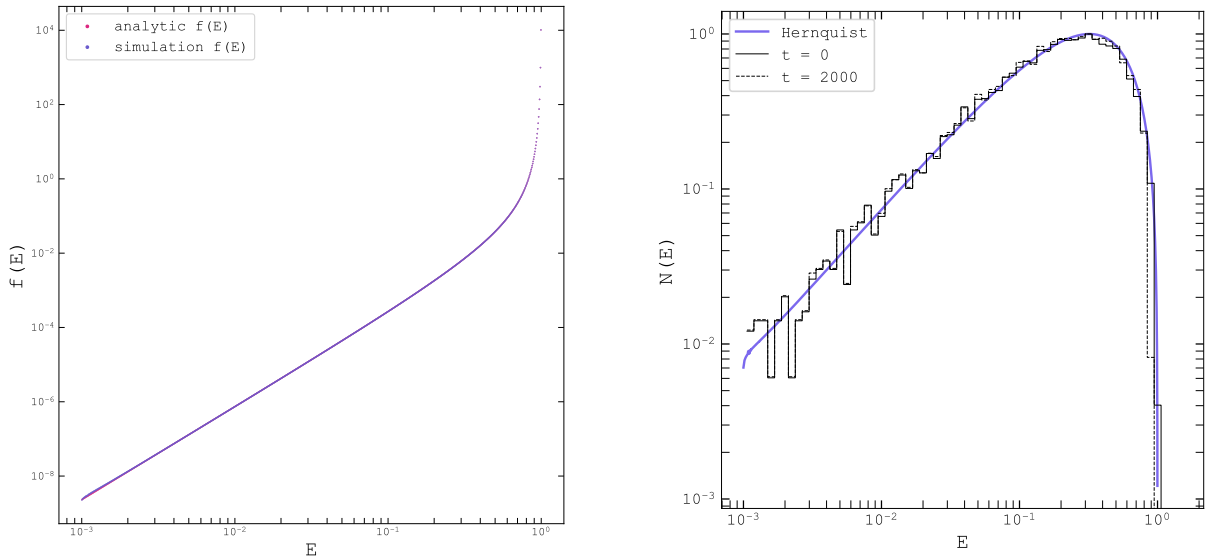


Figure 6. Left panel: Plots of the analytical and simulation energy Distribution Functions. The simulation distributions agree very well with the analytical expressions. Right panel: $N(E)$ distribution of a test Hernquist model in isolation at timesteps $t = 0$ and $t = 2,000$ overplotted with the analytical distribution of energies. After 2,000 iterations, the distribution of energies still closely follows the analytical model and has not deviated significantly from the initial energy distribution.

Agama python package (E. Vasiliev 2018) using the `SelfConsistentModel` class, which supports building multiple-component models using different potentials and distribution functions. A 'Quasi-Isothermal' disk potential and distribution function was chosen to model the galaxy, with a surface density $\Sigma_0 = 0.63$, a disk radius $R_d = 0.9$, a scale height $H_d = 0.15$, and a radial velocity dispersion of $\sigma_r \in [0.21, 2.35]$. These values were optimized to keep the disk as stable as possible,

with the Toomre stability parameter, Q in mind. For a stellar disk, this is defined as:

$$Q_{star} = \frac{\sigma_R \kappa}{\pi G \Sigma} \quad (12)$$

$$\kappa^2 = 2 \frac{v}{R} \left(\frac{v}{R} + \frac{dv}{dR} \right), \quad (13)$$

with κ defined as the epicyclic frequency (J. Binney & S. Tremaine 1987). For a stable disk in equilibrium, $Q > 1$. Agama samples the DF and generates a set of

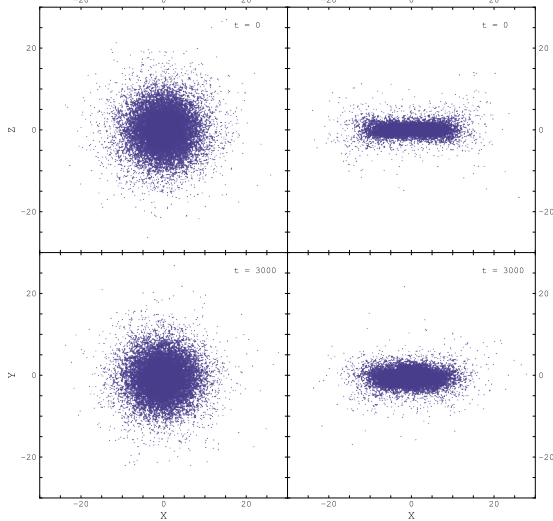


Figure 7. xy and xz projections of timesteps $t = 0$ and $t = 3,000$ of the disk galaxy evolving in isolation. There is obvious disk bulging from instabilities but the system is self-gravitating and in quasi-equilibrium.

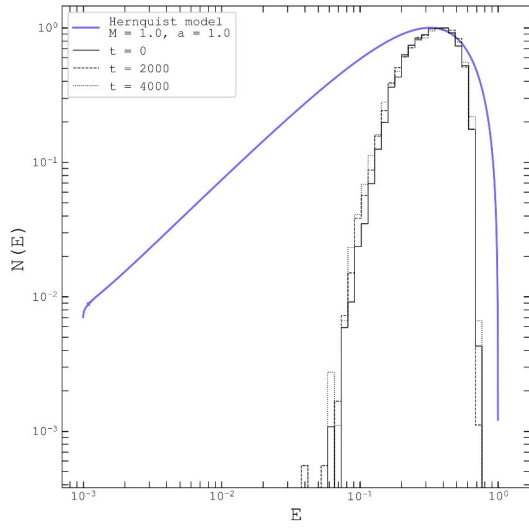


Figure 8. $N(E)$ distribution of a Hernquist profile overplotted with the $N(E)$ distribution of the disk galaxy in isolation at timesteps $t = 0, 2,000$, and $4,000$. Despite small fluctuations, the curves mostly converge, indicating the disk galaxy is self-gravitating.

initial phase space coordinates, which can then be used as our perturber galaxy. Disk galaxies, however, are numerically unstable and very sensitive to initial parameters, with effects such as disk heating, or the gradual growth of random velocities, and accumulation of numerical errors causing the initial disk to expand radially (J. Binney & S. Tremaine 1987). Integrating our model in isolation produces noticeable disk heating, with the

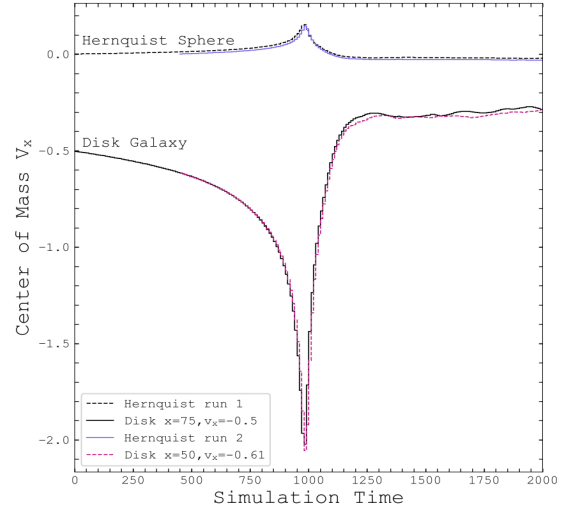


Figure 9. Center of mass velocity in the x direction plotted over simulation time units for the two different 10:1 radial test mergers. The Hernquist and disk galaxy v_{com_x} are overplotted with the initial run plotted in black and the second simulation in color. The velocities agree with only slight differences during the merger event at $t \simeq 60$, showing acceptable convergence. The effects of the 10:1 mass ratio are also of note, with the more massive Hernquist galaxy deviating only slightly from its initial center of mass.

initial thin disk morphing into a thicker disk, displayed in figure 7. Thicker disks have the advantage of being much more stable numerically, despite being physically less realistic. Yet after many timesteps, all the particles in the disk are still bound and self-gravitating in some quasi-equilibrium state. Plotting a log distribution of the energies (figure 8) across 4,000 timesteps reveals acceptable convergence between the initial state and after numerous galaxy rotations, indicating the disk model is self-gravitating and confirming quasi-equilibrium. The Hernquist model energy curve is also plotted for reference, and is notable for having a much broader range of acceptable energies than a disk in equilibrium.

2.6. Simulation Convergence

Because of heavy computational time, it is important to investigate the dependence on initial distances between the satellite and host galaxies. While placing the perturber many scale radii away from the host galaxy is more physically accurate, it would greatly increase computational time during the lead-up to the merger. Too small an initial separation could heavily bias the results, leading to greater divergence between small differences in initial conditions. To choose an optimal and consistent starting point, a simple 10:1 merger was simulated, where a Hernquist sphere was placed at rest on the origin in a radial collision path with a disk galaxy 75 simulation units away. The disk was given a velocity of

$v_x = -0.5$, corresponding to slightly less than the escape velocity at that distance. The velocity of the disk's center of mass was recorded at a distance of $x = 50$, and again at $x \simeq \alpha$, when the galaxies start merging. A second test was conducted with an identical setup, but this time the disk was moved to a position of $x = 50$ and given the velocity recorded from the previous run at this position. Figure 9 plots the magnitude of the center of mass velocity in the x direction for both galaxies, plotted over simulation timesteps. At a simulation time of $t \sim 800$, the two galaxies start to merge in both runs. The disk galaxy's $v_{com,x}$ becomes increasingly negative until $t \sim 1,000$, where it crosses through the Hernquist galaxy center, and subsequently becomes pulled back towards the more massive Hernquist galaxy. The two runs agree quite closely, showing the two simulations converged. From this test, we can assume simulation results are irrespective of the initial separation distance up to $R \simeq 50$ units, and all subsequent tests take on this initial distance.

3. PRELIMINARY RESULTS FROM THE MERGER SIMULATIONS

Based on the work done by E. Iodice et al. (2017), we investigated the merger between a giant, early type, spherical galaxy and a smaller disk galaxy with a mass ratio of 10:1. For all runs this mass ratio was assumed between the two galaxies. A total of three simulation runs were computed to more properly search simulation space, with varying parameters. The mergers are characterized by collision paths that are either purely radial or include a small impact parameter, with disk inclinations varying from edge-on to face-on. The choice for simulating mostly radial mergers is grounded on the observed merger remnants seen in the inner spheroid of Fornax A, which are distributed radially along the galaxy. The spherical symmetry of the Hernquist sphere also greatly simplifies the initial setup and allows us to place the disk galaxy solely along the x -axis for radial mergers. All simulations were run on the Yale Astronomy department computer cluster, which greatly sped up calculations and allowed for a massive increase in particles, and hence simulation resolution. All simulation parameters are listed in Table 1.

3.1. Merger Initial Conditions

In all simulations, the Hernquist sphere was initiated with a mass of $M = 10$, and a scale radius of $\alpha = 2$. In each subsequent run, the number of particles N was increased to push the limits of our simulations. Each simulation adopts the Hernquist sphere's frame of reference, placing it at rest on the origin. The disk galaxy

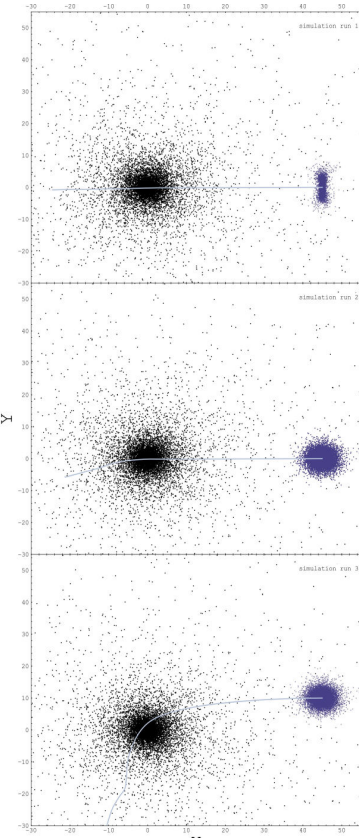


Figure 10. xy projections of the initial conditions overplotted with the perturber galaxy's center of mass trajectory.

was generated with a total mass $M = 1$, and scale radius $\alpha \sim 3$ using the parameters outlined in section 2.5. Its center of mass was given an initial velocity pointing in the direction of the Hernquist galaxy with a magnitude slightly less than the escape speed. The first run investigated the effects of a radial, face-on merger with a total particle count of $N = 23,000$ split between the two galaxies. The perturber disk consisted of 10,000 particles and was placed 50 simulation units away from the Hernquist sphere on the x -axis with an initial velocity of $v_x = -0.5$. The disk inclination was set to produce a face-on merger configuration. In the next two runs, the particle count was increased for a higher resolution at the cost of slightly longer computational times. The second simulation run investigated the case of an edge-on, radial merger, with a total particle count of $N = 26,000$ distributed evenly across both galaxies. Similarly to the previous run, the disk was placed 50 units away with a COM velocity $v_x = -0.5$. In the third simulation run, the particle count was increased to $N = 130,000$, assigning 80,000 particles to the disk to improve the resolution of the merger remnant. The disk was given a slight impact parameter by placing it 50 units away in the x direction and 10 units in the y direction. The inclination was set up to be edge-on and once again the

Table 1. Perturber Galaxy Initial Conditions

Simulation Run	M	$N_{\text{perturber}}$	$N_{\text{simulation}}$	Initial Position (x, y, z)	Initial Velocity (v_x, v_y, v_z)	Disk Inclination
I	1	10,000	23,000	(50, 0, 0)	(−0.5, 0, 0)	Face-on
II	1	13,000	26,000	(50, 0, 0)	(−0.5, 0, 0)	Edge-on
III	1	80,000	130,000	(50, 10, 0)	(−0.5, 0, 0)	Edge-on

NOTE—For each simulation run, the mass ratio between the spherical galaxy and the perturber is 10:1. The spherical galaxy differs across each run only in its number of particles. The total perturber galaxy mass M is given in simulation units. $N_{\text{simulation}}$ specifies the total number of particles N of both galaxies.

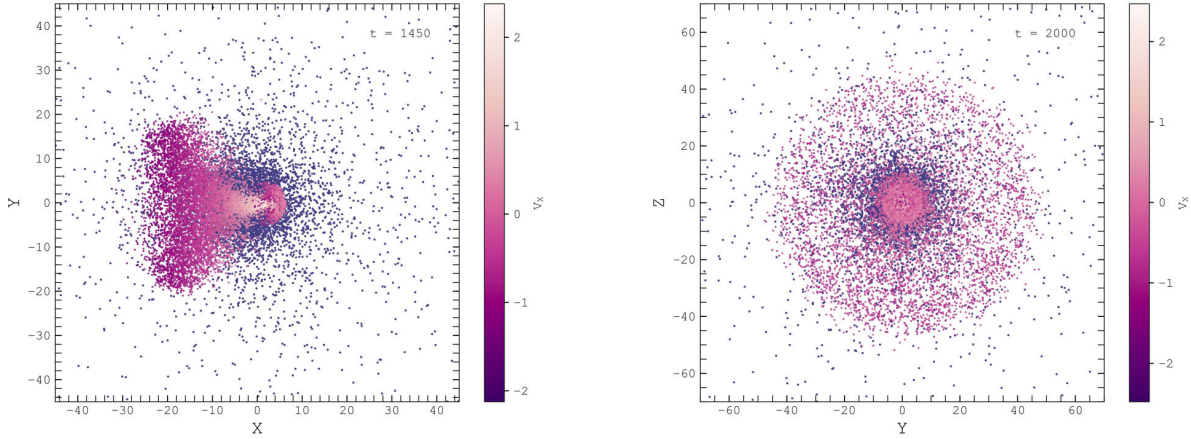


Figure 11. Left panel: xy projection of the face-on radial simulation at the height of the merger event. The disk particles are colored by their x velocity (radial) component. Right panel: yz projection at a slightly later time showing most of the disk particles relaxed in the center of the Hernquist sphere. The remainder of the particles extend radially out in the yz plane. The perturber particles (pink) are plotted on top of the host galaxy (dark blue) for clarity.

COM velocity was set to $v_x = -0.5$. For all mergers, the timestep was set to $dt = 0.05$, and the softening length was determined by equation (2). Each simulation was evolved for approximately 5-7,000 timesteps to properly assess the merging and relaxation process. The initial simulation configurations are shown in figure 10. The COM position of the disk galaxy throughout the simulation is overplotted in each frame to show the trajectory of the perturber for each setup.

3.2. Simulation Run 1

In the case of the face-on, radial merger the galaxies begin interacting strongly at a simulation time $t \sim 1,100$, where the disk begins to bunch up into an elongated spheroid (see timestep 1,100, figure 12, left panel) before being ejected out of the host galaxy at a high velocity. A distinctive conical-shaped remnant is formed extending radially in the negative x direction, initially dispersing most of the disk particles. However, a portion of the disk is trapped under the gravitational potential and is seen oscillating radially in figure 11 (left panel), with complex kinematics causing shells of particles overturning onto themselves. The disk particle's colors are mapped

to the radial component of their velocities, clearly showing particles at similar x coordinates traveling in opposing directions. Yet this behavior is short-lived lived with many of the central particles settling into the new potential after ~ 300 timesteps. Viewed from the yz plane (Figure 11, right panel), the axisymmetry of the disk is retained in the merger remnant, yet the angular momentum from the disk rotation seems to have been lost. Many of the particles ejected out in the yz plane are also seen decelerating before reaching zero velocity and falling back into the host galaxy, as expected for a radial merger. Although interesting, the merger remnant does not match the more elongated filaments and clumps observed in Fornax A, suggesting the perturber galaxy likely collided more edge-on.

Phase space diagrams of the disk merger remnants are helpful tools for further comparing the simulation results to the merger remnant found in NGC 1316. A thin cross-section of the disk remnant is chosen, typically along its major axis, and flattened into a 1-dimensional array. The component of their velocities along some line of sight, unit vector of interest (v_{los}), is then com-

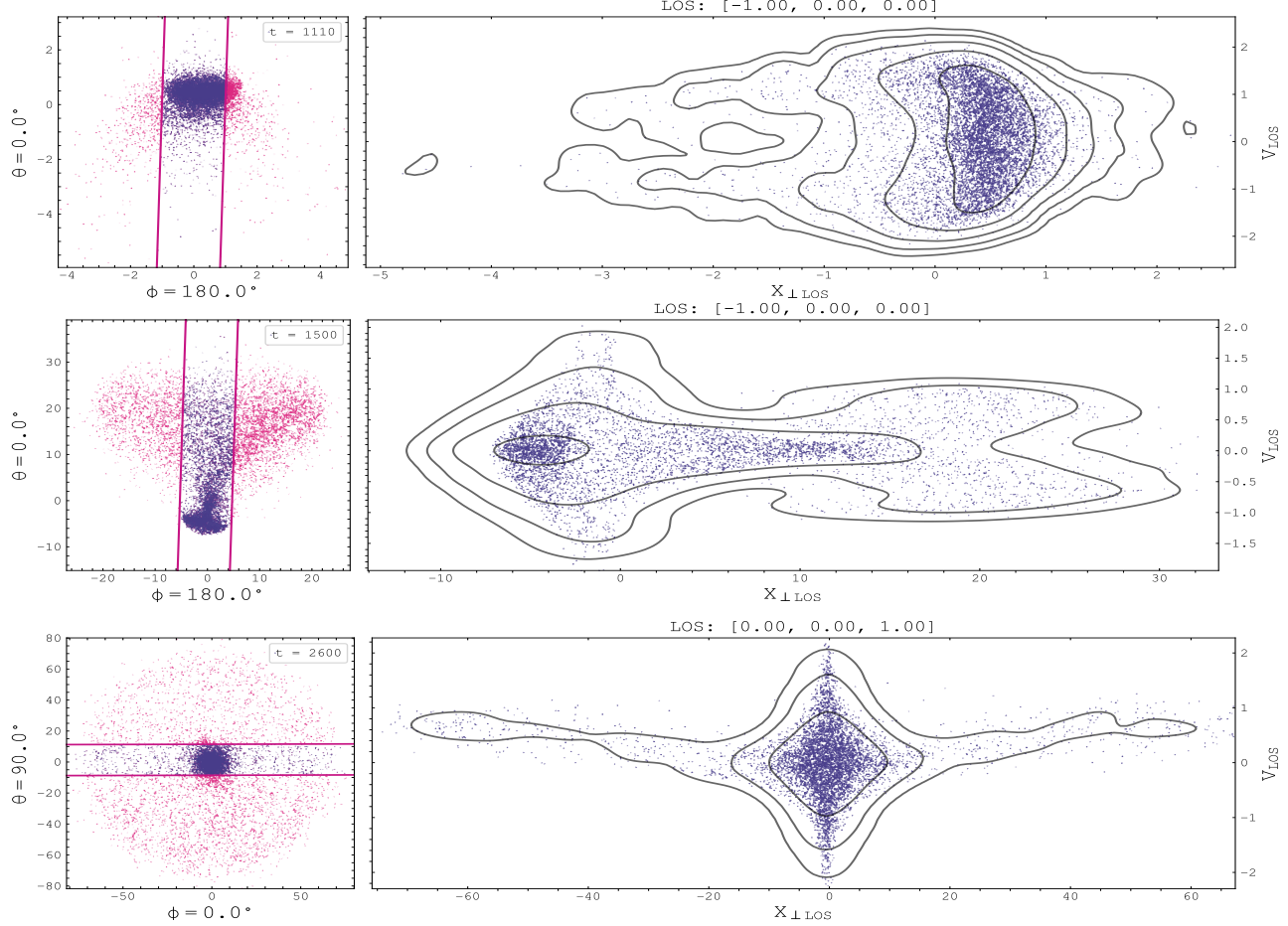


Figure 12. Position–velocity diagrams of the perturber galaxy in simulation 1 along varying lines of sight and at different timesteps. The top two panels correspond to projections along the $-\hat{x}$ direction, while the bottom corresponds to the \hat{z} direction. Left panels show real-space views, and right panels show phase-space views.

puted through a dot product, allowing us to make position v. velocity diagrams of the simulation. Particles with positive v_{los} are moving away from the line of sight, while negative velocities indicate motion towards the ‘observer’. Figure 12 displays a collection of time-series phase diagrams of simulation 1, for different line of sights and timesteps. Each phase space diagram also includes a plot of the disk remnant in real space along the line of sight for reference, as well as the cross-section of interest, marked by the parallel pink lines. Right before the merger, the disk is rotating in the yz plane and traveling along the x direction, with all the particles traveling towards the Hernquist sphere at high velocity towards the $-\hat{x}$ direction. Immediately after the impact ($t = 1,100$), the disk has become squished into a tight elongated spheroid by the potential of the Hernquist sphere, displayed in the topmost plot of Figure 12. The kinematics of the merger debris is now more complex, with large differences in velocity magnitude and direction for particles at similar positions, as they os-

cillate radially and form shells (see figure 11). As the simulation progresses, most of the particles relax into a centrally concentrated merger remnant ($t = 1,550$) with the rest forming the conical tail apparent in figure 11, right panel. The central spheroid displays symmetry in its phase space diagram corresponding to the particles settling into the new potential field. The final merger remnant projected on the yz plane is displayed on the bottom panel of figure 12, showing a dense, centrally concentrated bulge in phase space with two long tails. These two diverging tails have a slight inclination, starting with a positive v_{los} at large radii and slowly decreasing in magnitude before becoming negative towards the base of the tails. This corresponds to the outermost particles slowly losing kinetic energy before coming at rest and eventually sinking back into the central core.

3.3. Simulation Run 2

In the second simulation run, the satellite galaxy was rotated 90° to be edge-on to the Hernquist sphere, such

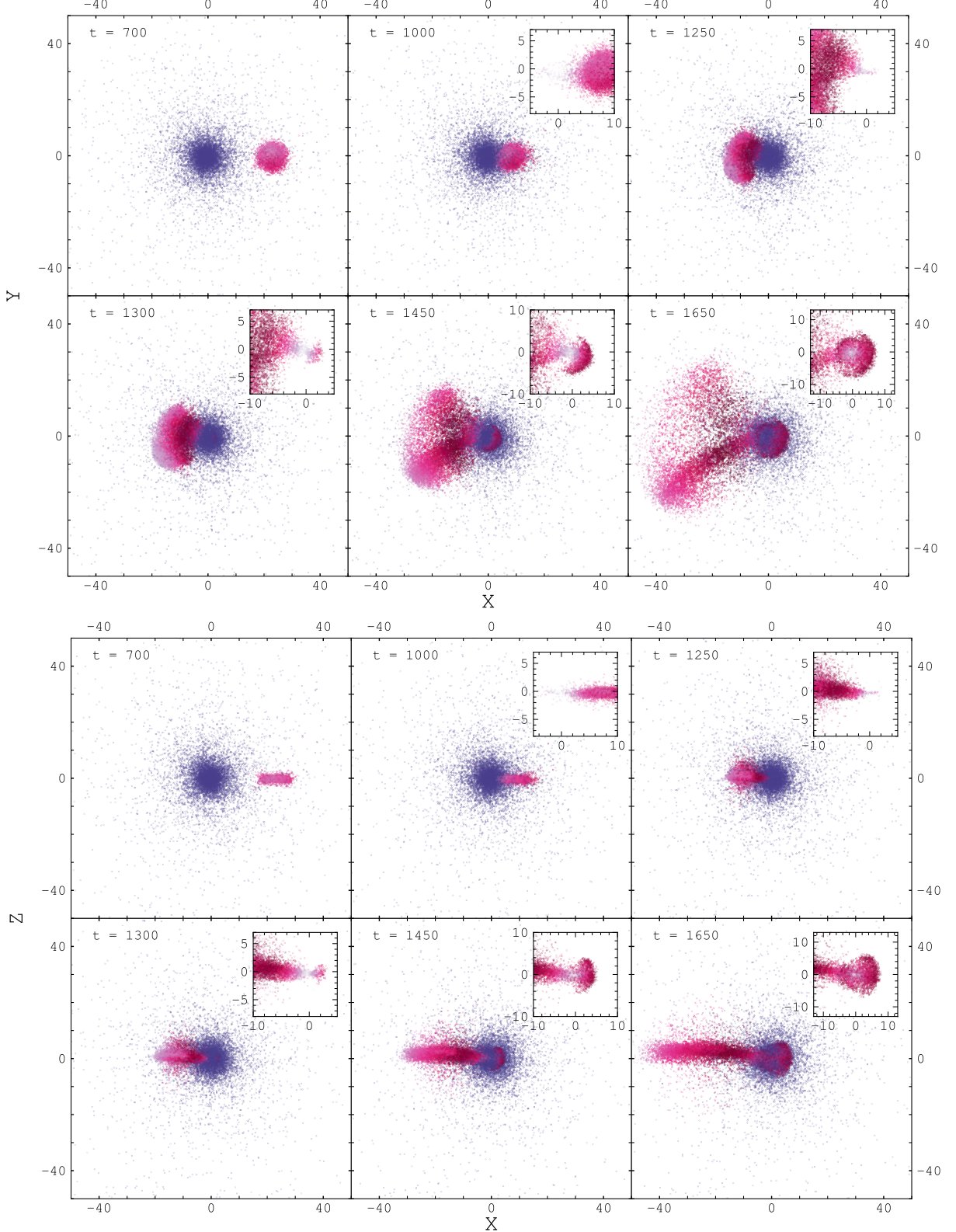


Figure 13. Top panel: xy projection of the first 1,650 timesteps of simulation 2. The perturber galaxy is also plotted in isolation to highlight structures otherwise obscured by the spherical component. The development of two distinct tidal tails extending from the central spheroid becomes evident in the final two snapshots. The violent oscillations present in the central bulge are also in full view. Bottom panel: xz projection of the same timesteps. The perturber galaxy is also plotted in isolation to highlight structures otherwise obscured by the spherical component. The merger remnant is clearly confined to the xy plane, with little to no vertical z motions. The distinctive radial oscillations and shells are also apparent after $t = 1,300$. The spherical galaxy is plotted in dark blue, while the perturber galaxy is mapped to its velocity magnitude, with lighter colors corresponding to greater velocities.

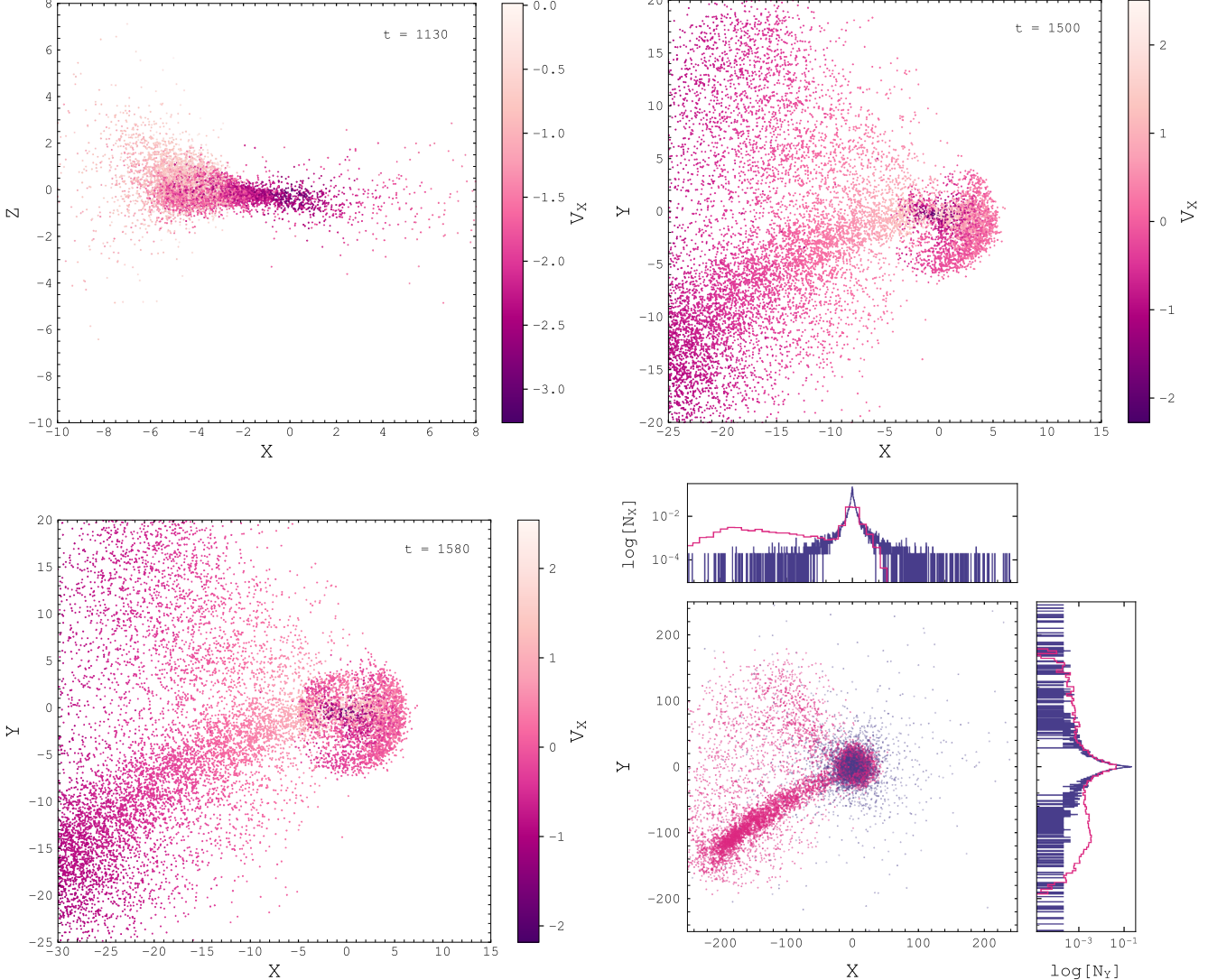


Figure 14. Closeup projections of the disk debris throughout the merger. The color is mapped to the radial velocity component v_x , showing the complex kinematics of the merger. Panels correspond to timesteps 1,100, 1,500, 1,580, and 5,354, respectively. Note the different projections used for the vertical axis.

that the surface normals of the galaxies were perpendicular to each other. The galaxies began merging at $t \sim 1,000$. Unlike the face-on, radial merger, which spread out axisymmetrically in the yz plane (figure 11, right panel), the remnant formed throughout this simulation is more elongated with a distinct tail extending in the xy plane and curving towards the $-y$ direction. A small fraction of the particles are also seen forming a smaller, less dense tail, seen in figure 13, top panel, at $t = 1,450$, traveling in the opposite direction. This smaller, tail-like structure is short-lived, dispersing into a less dense field of particles some ~ 200 timesteps later. Considering the perturber galaxy's trajectory was solely in the $-x$ direction, the merger remnant should oscillate back and forth on the x -axis. Yet the presence of the large

tail curving outwards can perhaps be explained by the rotational energy of the disk deviating the particles off-course. This is supported by the fact that the direction of the disk's rotation pointed in the same direction as the tail. Many of the particles in the tail have reached escape velocity and travel at high speed away from the central spheroid throughout the simulation. This is apparent in figure 14, bottom-right panel, which shows the final simulation snapshot of this run. The tail extends a couple of hundred simulation units from the sphere, with many of the particles having attained escape velocity.

Rotating to the xz frame of reference (figure 13, bottom panel), the dispersion of the particles is much tighter with the majority concentrated in the elongated tail extending in the $-x$ direction. The disk is stretched

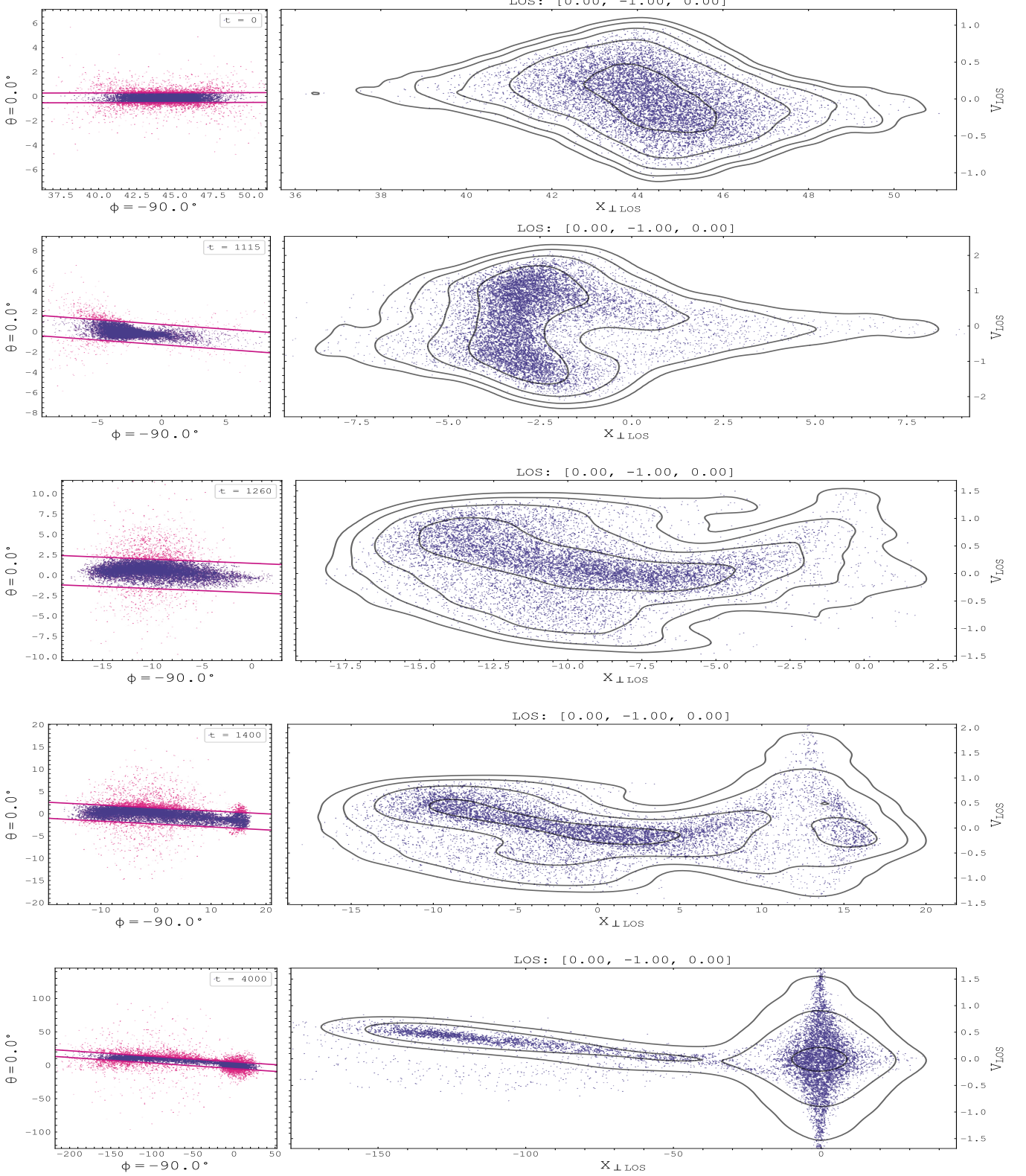


Figure 15. Position v. velocity evolution of simulation 2 in the xz projection, along the $-\hat{y}$ line-of-sight vector. The panels show the system's evolution from $t = 0$ to $t = 4,000$. Notice the striking similarities between the NGC 1316 PVD (figure 1) and the final timestep. In both, the phase-space distribution is elongated across two opposing quadrants, and for a given position along the major axis, multiple clumps appear at distinct line-of-sight velocities. This structure is evidence of a highly radial merger, producing irregular orbits rather than a planar, disk-like rotation.

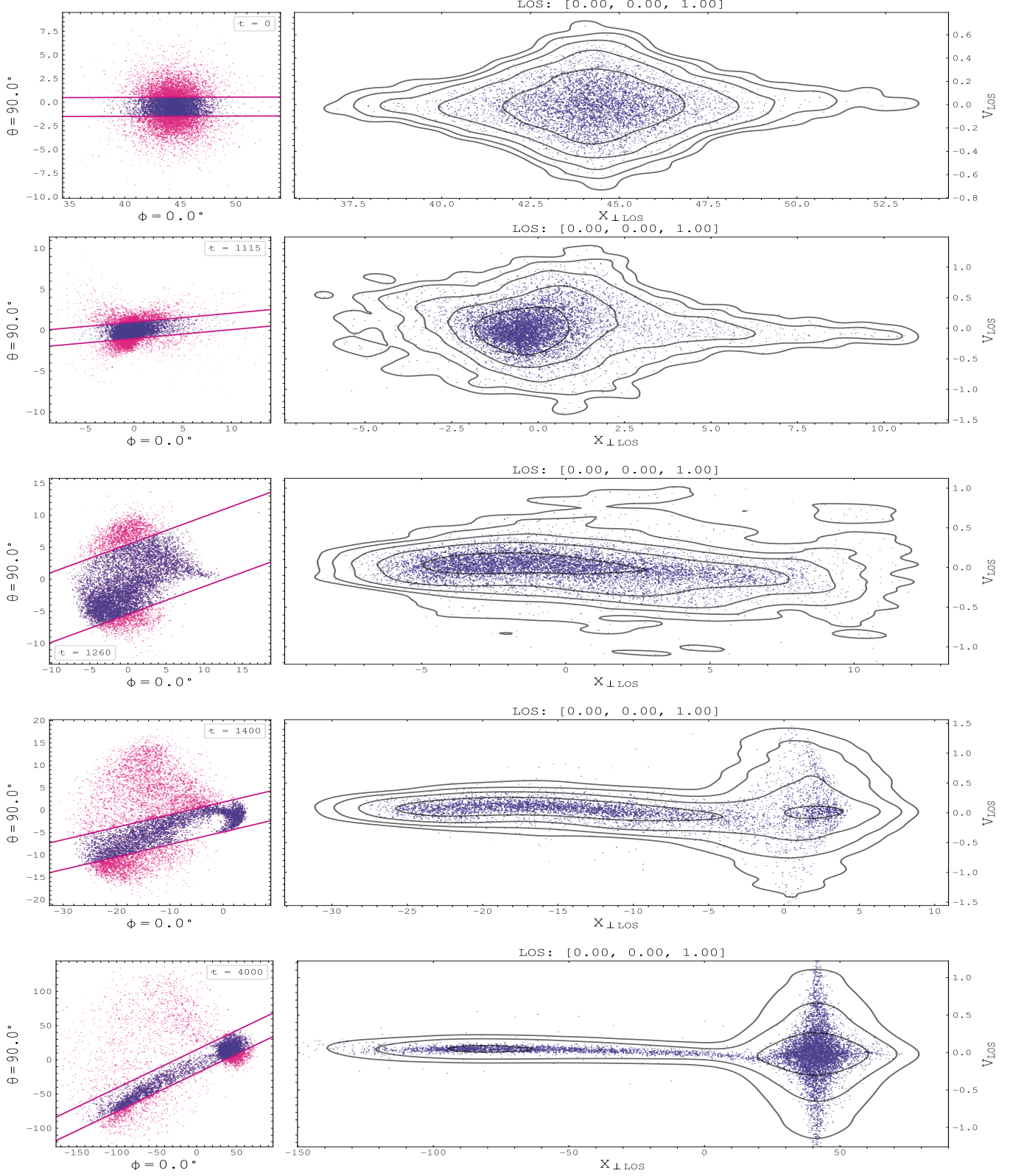


Figure 16. Position–velocity evolution of simulation 2 in the xy projection, viewed along the \hat{z} line of sight. The panels track the same timesteps as those in Figure 15. The nearly flat phase-space distribution indicates little to no motion along \hat{z} , with most particles confined to the xy plane. Only the central core exhibits vertical motions, driven by particles settling into the newly formed potential.

as it approaches the Hernquist sphere ($t = 1,000$), until it crosses the center and subsequently accelerates outwards with some vertical motions ($t = 1,250$). This increase in vertical velocity is apparent in figure 14, top left panel, where many of the particles are ejected upwards a couple times the disk scale height. The particles now closest to the center of the spherical galaxy are pulled back in and start to oscillate, forming irregular, spherical shells of radius $r \sim 5$ units (figure 14, at $t = 1,580$). Particles near the center continue to oscillate violently in the core before they start to settle into the spheroidal remnant. The plots in figure 14 display close-ups of different simulation snapshots of the central region, with the color mapped to the particles' velocity component along the radial direction. Figure 14 at timesteps $t = 1,500$ and $1,580$ is particularly interesting, with the large stellar shells in full view as they loop around the center of the spheroid. The disk debris seems to oscillate 3-4 times about the center of the Hernquist galaxy before settling into a tight ball of particles. At timestep 5,354 (figure 14, bottom right), corresponding to the end of the simulation, the central bulge of particles is now mostly spheroidal and has grown considerably ($r \sim 25$). The plot also displays the log-scaled, normalized number density distribution of each galaxy on the side panels. The Hernquist galaxy distribution seems mostly unaffected, its central density peak having deviated only slightly from the origin. On the other hand, the merger debris of the disk is much more irregularly spread out, with the tail distributions clearly displayed. The disk galaxy remnant density is highest at the center, where many of the particles merged with the spherical galaxy, followed by the 'third quadrant' of the plot corresponding to the tail.

Studying the evolution of the phase space of the disk galaxy throughout the simulation reveals similarities to NGC 1316. Figure 15 shows the xz projection along the $-\hat{y}$ line-of-sight vector. At $t = 0$, the phase space shows an asymmetrical diamond-shaped distribution, arising from half the disk rotating towards the observer and the other half rotating away. As the violent merger unfolds, the phase space distribution becomes increasingly irregular, morphing into a thin distribution elongated across two opposing quadrants (see figure 15, $t = 4,000$). In addition, along the major axis, there are multiple clumps of particles with varying line-of-sight velocities, indicative of mergers with highly radial trajectories. With both of these attributes present in the NGC 1316 phase space diagram as well as similarities in the real space projection distributions (figure 1), the violent merger experienced by NGC 1316 was likely highly radial. The real space projections share similarities in their distri-

butions as well. The phase space evolution in the xy plane along the \hat{z} line-of-sight vector (figure 16) depicts a similar evolution as seen in figure 15, but highlights the absence of vertical \hat{z} motions by the disk remnant.

3.4. Simulation Run 3

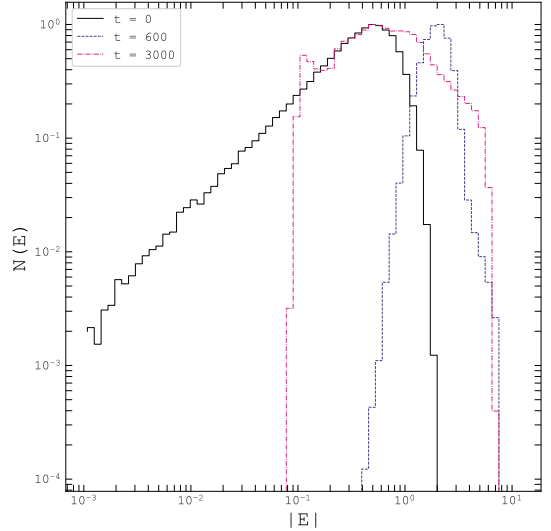


Figure 17. Log-log $N(E)$ plot of the perturber galaxy energies during the simulation. As expected, the $t = 0$ curve shows a broad energy range (albeit narrower than a Hernquist galaxy distribution). At the height of the violent collision ($t = 600$), the energy profile tightens, with particles excited to higher energies before broadening out into a more smooth distribution. Note the absolute values of the energies are plotted.

The third and final simulation run differed from the first two by having a non-zero impact parameter. The simulation setup was identical to simulation 2, but with the perturber galaxy given an initial y coordinate of 10 simulation units. With an order of magnitude more particles, a hexbin plot (Figure 18) reveals the structure inside the merger remnant, where particles are binned by localized density. The effects of the impact parameter are seen in the merger remnant tail, which has rotated counterclockwise with respect to the tail in simulation 2. Viewed at times 790 and 1,190, the tail has completed almost a full 180° rotation about the central core—a property not seen in the fully radial mergers. This implies some of the angular momentum from the disk rotation is kept in the merger remnant, creating loops of debris rotating around the center (see $t = 3,180$). This central spheroid is also much larger and more spherically symmetric, with large, distinct shells of stellar particles orbiting around the central spheroid. The evolution of the tail and stellar shell formation are displayed in fig-

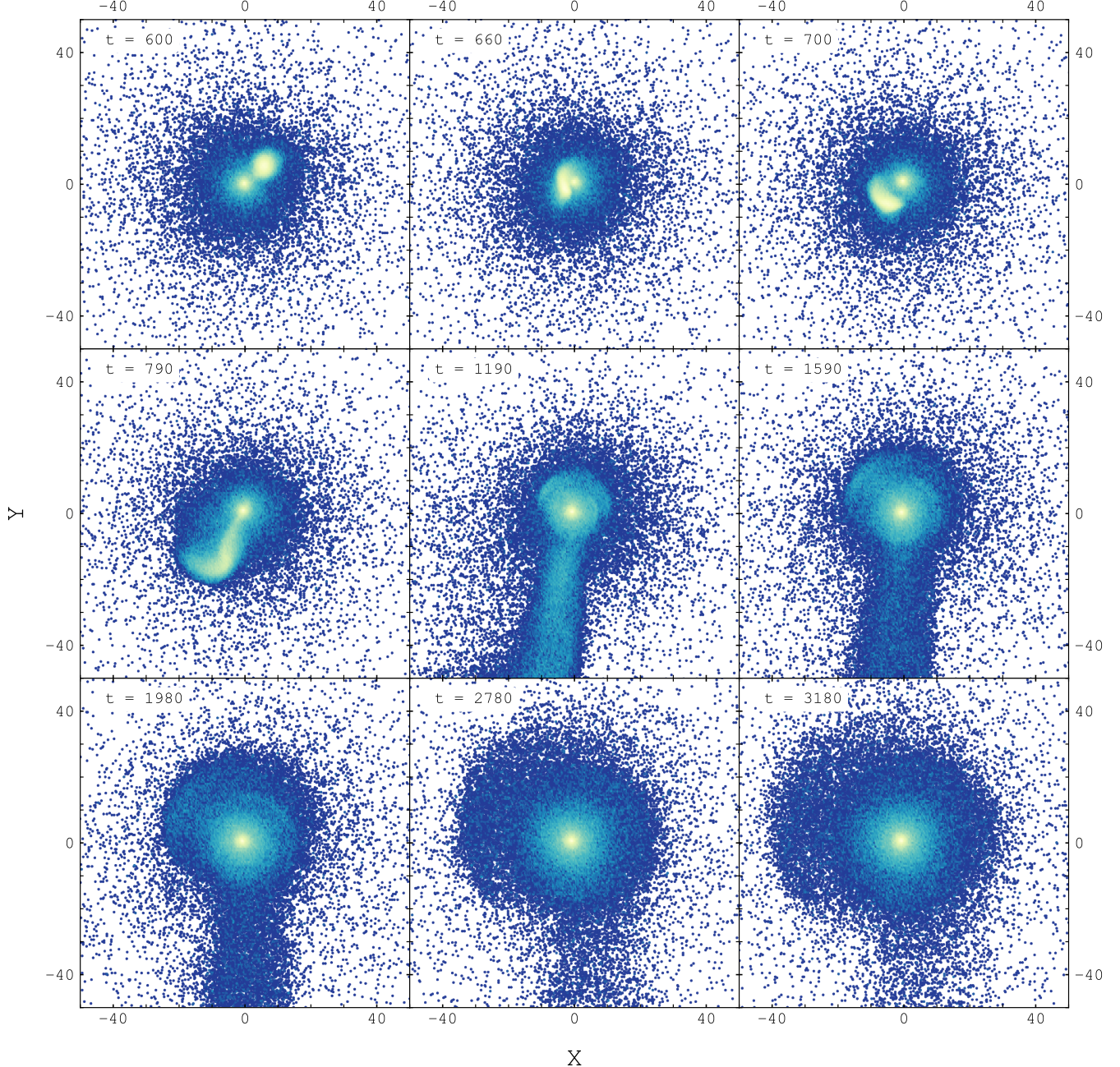


Figure 18. Hexbin plot of the third simulation in the xy projection throughout various timesteps. The particles are binned by localized number density to show the internal structure of the merger remnant. Note the spherical shells of stellar debris orbiting the central core towards the end of the simulation. The particles of both galaxies are binned together. Brighter colors are mapped to regions of higher density in this plot.

ures 19 and 20, which show a zoom-in of the merger remnant. These show similar timesteps to figure 18 but keep the galaxies plotted in separate colors for clarity. Plotting the snapshots on the yz plane (Figure 21) reveals a large range of vertical motion not present in the edge-on simulation. In Figure 17, the energies of the perturber at different timesteps are plotted on a log-log plot. As expected, the initial disk is narrower than

the analytical Hernquist profile (see figure 22 in the appendix), yet becomes even narrower during the initial collision ($t = 600$) before broadening into a smoother distribution. Comparing simulation 3 to simulation 2, the effect of the impact parameter is clearly visible. The stellar loops and shells are much more pronounced with the presence of the impact parameter, recovering some of the structure seen in NGC 1316. The phase-space of

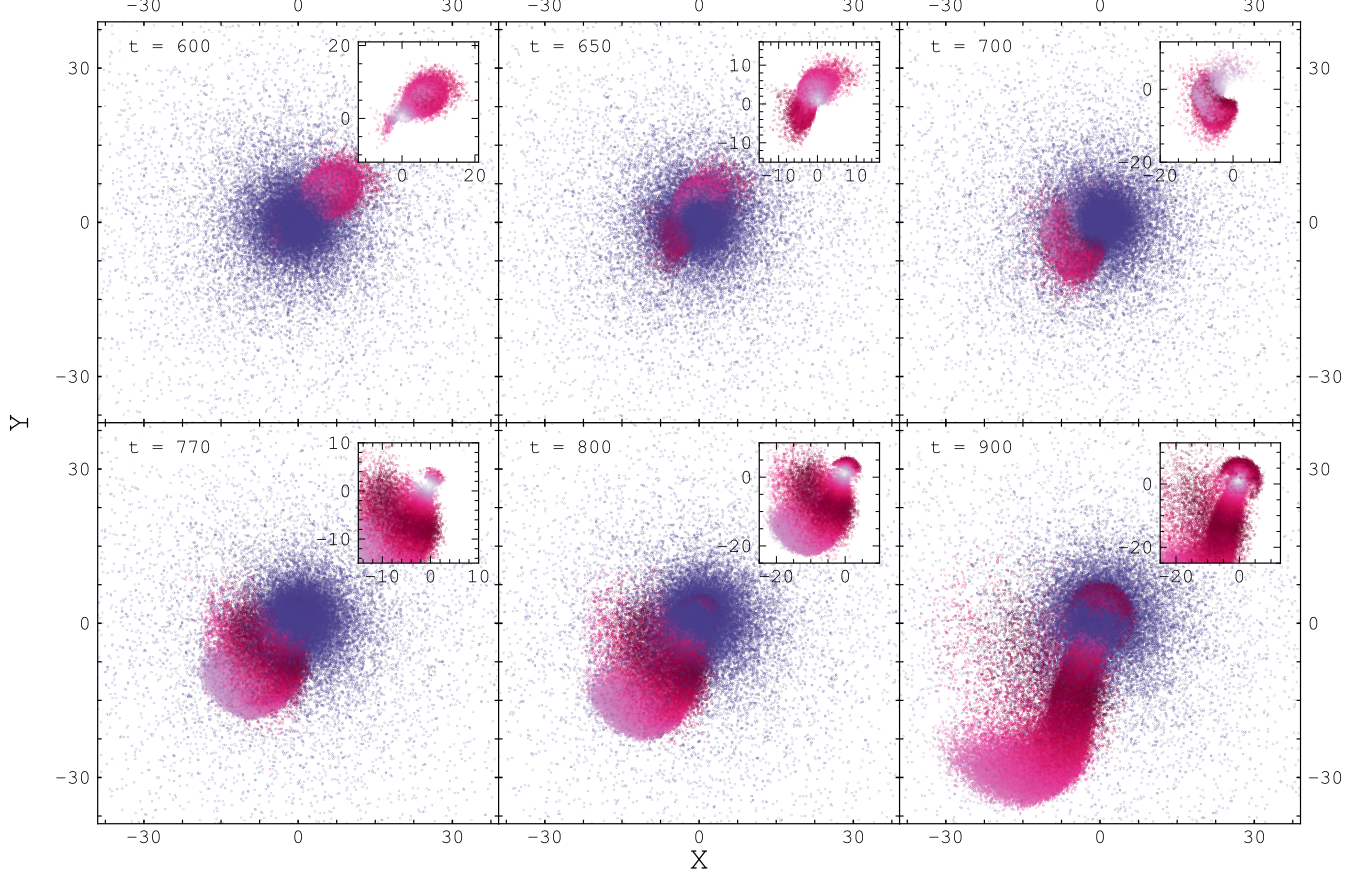


Figure 19. xy projection of the simulation central region at the height of the collision. The tail forming process is clearly visible. The perturber galaxy is also plotted in the inset axes for clarity, with its color mapped to its velocity magnitude. Here, lighter colors are mapped to larger velocities.

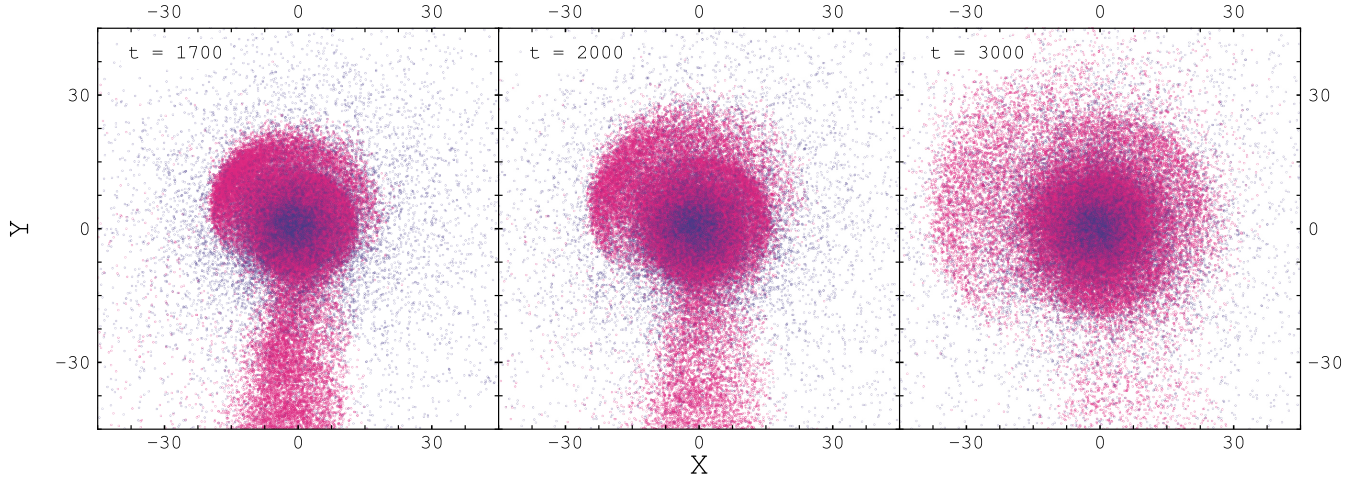


Figure 20. Evolution of the spherical shells towards the late stages of the simulation. The shells start forming loops of stellar debris as they orbit the central spheroid.

the perturber in simulation 3 shares similarities to simulation 2, with a long tail extending out from the central spheroid (see figure 25 in the appendix). Figure 23, dis-

plays the final remnant as seen from the xy plane. The number density of the disk particles is much less evenly distributed in the y direction when compared to the fi-

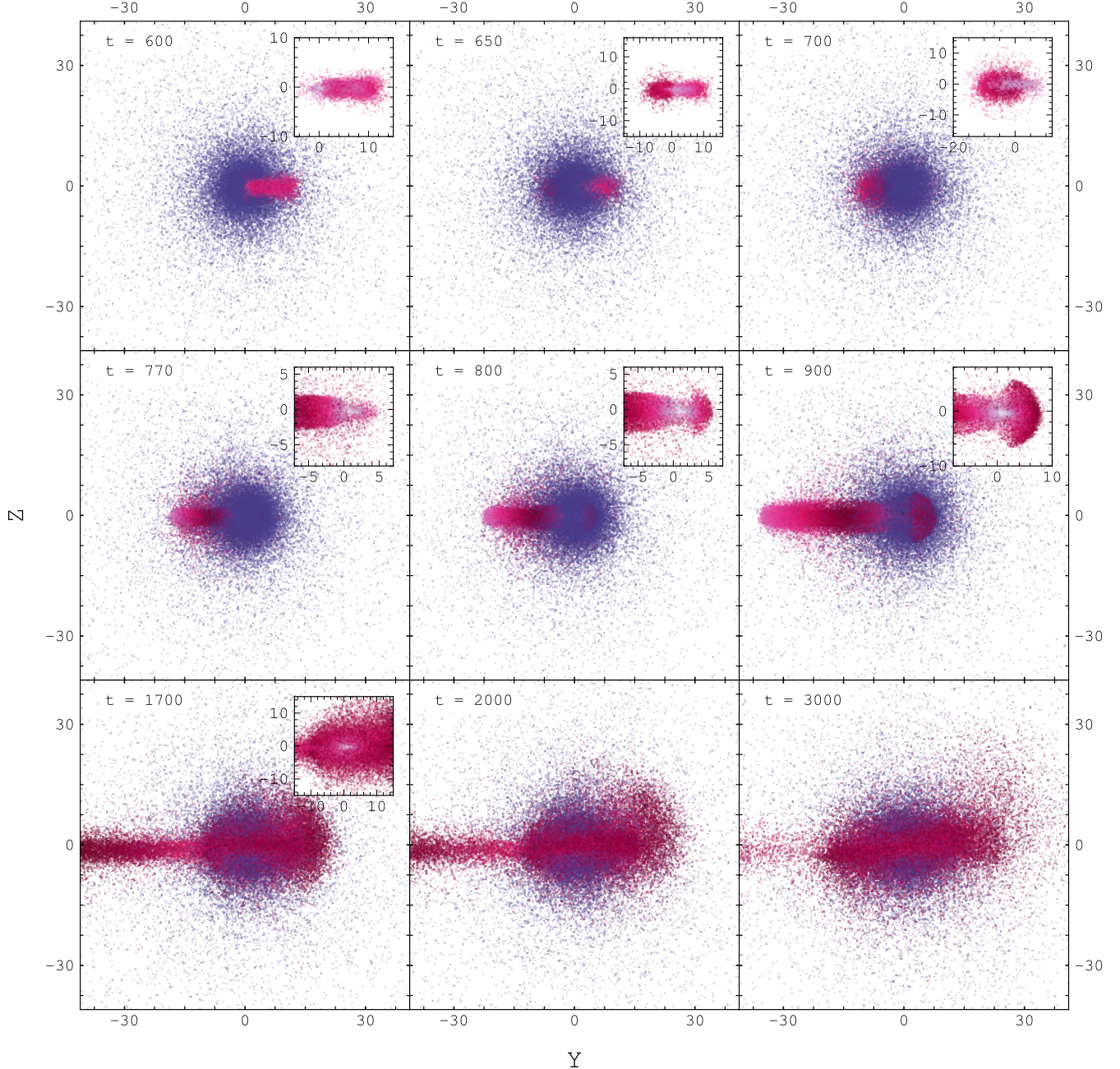


Figure 21. yz projection of the simulation showing the system before, during, and after the violent collision. Note the much larger vertical extent of the particles as they form shells around the central core. Each particle of the perturber galaxy is mapped to its velocity magnitude, with lighter colors corresponding to larger velocities.

nal distribution of simulation 2 (Figure 14, right panel), with most of the particles having a negative y coordinate. The density in the x direction however, agrees more closely between the two runs.

4. CONCLUSION

Although far from accurately simulating NGC 1316, with the simulations suffering from an extremely low particle count and missing important components such

as dark matter, gas, and a central bulge, these simulations offer some insight into the effects of gravity onto collisionless radial mergers. The merger remnants of the radial cases have elongated, continuous distributions similar to the CO distribution seen in Fornax A. Simulation 2 phase-space diagrams show particle distributions similar to NGC 1316 observed phase-space distributions, while simulation 3 recreated the stellar loops and shells seen in the central core of NGC 1316. The

simulations ran in this project are in favor of the perturber merging with NGC 1316 having a highly radial component, possibly with a small impact parameter, although this needs to be investigated more. Parameter space is very large and there are many more combinations of impact parameters, initial velocities, and disk inclinations to simulate. In the future, I hope to continue to optimize the code, such as looking into tree

code algorithms to support orders of magnitude more particles.

5. ACKNOWLEDGMENTS

I would like to thank Professor Jeffrey Kenney, Professor Marla Geha, and Shashank Dattathri for providing invaluable help in completing this project. This would not have been possible without them. I would also like to thank my Astro Big-Sib Sebastian Monzon and Barry Chiang for helping me out with running the simulations. Their help proved invaluable in finishing this thesis project.

REFERENCES

- Binney, J., & Tremaine, S. 1987, Galactic Dynamics (Princeton Series in Astrophysics)
- Dehnen, W. 2001, Monthly Notices of the Royal Astronomical Society, 324, 273,
doi: [10.1046/j.1365-8711.2001.04237.x](https://doi.org/10.1046/j.1365-8711.2001.04237.x)
- Iodice, E., Spavone, M., Capaccioli, M., et al. 2017, ApJ, 839, 21, doi: [10.3847/1538-4357/aa6846](https://doi.org/10.3847/1538-4357/aa6846)
- Kenney, J.D.P. 2025, placeholder
- Lanz, L., Jones, C., Forman, W. R., et al. 2010, The Astrophysical Journal, 721, 1702,
doi: [10.1088/0004-637X/721/2/1702](https://doi.org/10.1088/0004-637X/721/2/1702)
- Maccagni, F. M., Murgia, M., Serra, P., et al. 2020, A&A, 634, A9, doi: [10.1051/0004-6361/201936867](https://doi.org/10.1051/0004-6361/201936867)
- Richtler, T., Hilker, M., Kumar, B., et al. 2014, A&A, 569, A41, doi: [10.1051/0004-6361/201423525](https://doi.org/10.1051/0004-6361/201423525)
- Schweizer, F. 1980, ApJ, 237, 303, doi: [10.1086/157870](https://doi.org/10.1086/157870)
- Vasiliev, E. 2018, Monthly Notices of the Royal Astronomical Society, 482, 1525,
doi: [10.1093/mnras/sty2672](https://doi.org/10.1093/mnras/sty2672)

6. APPENDIX

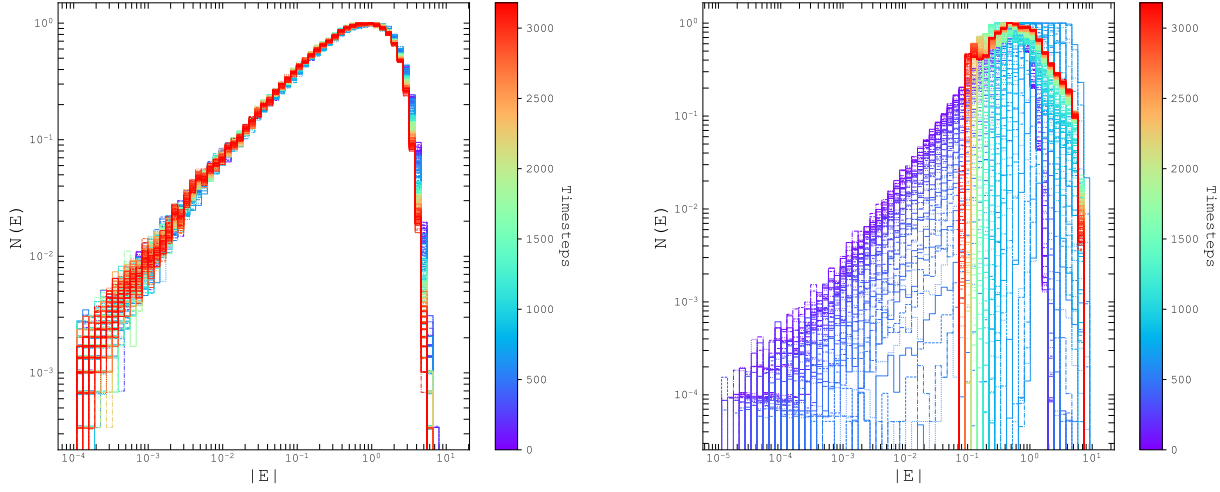


Figure 22. Evolution of the $N(E)$ curves of both the spherical (left panel) and perturber galaxy (right panel) during simulation 3. The curves are plotted at every timestep, with the color corresponding to the timestep of the simulation. Notice how the spherical galaxy's energy profile stays mostly constant throughout the violent simulation, due to its much higher mass. Note that the absolute value of the energies are plotted.

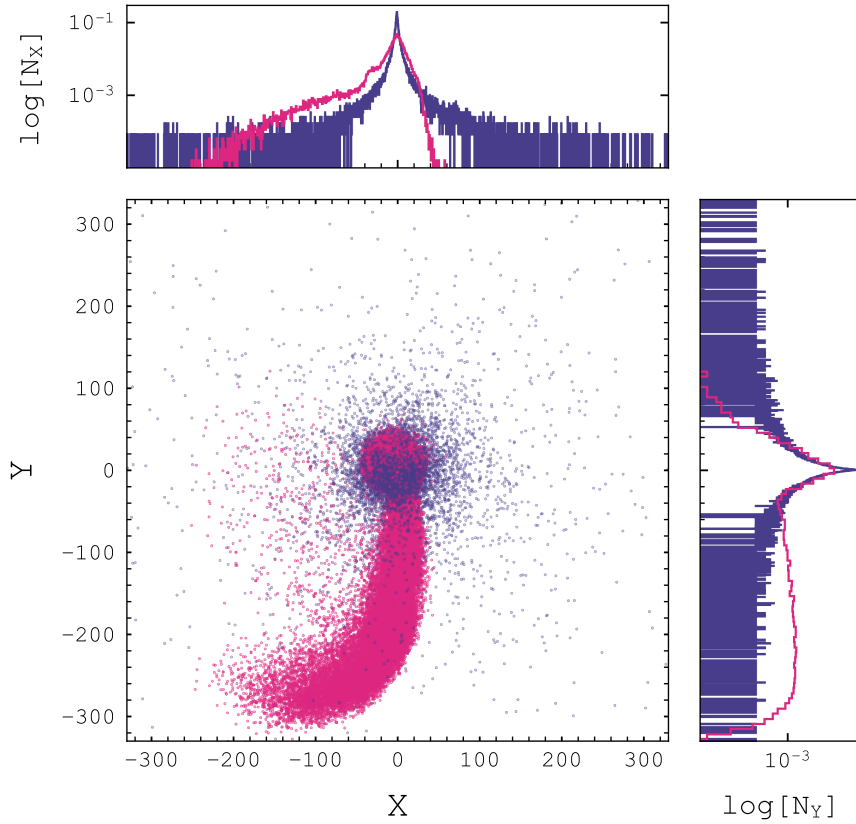


Figure 23. Final xy projection of simulation 3, with log density side plots.

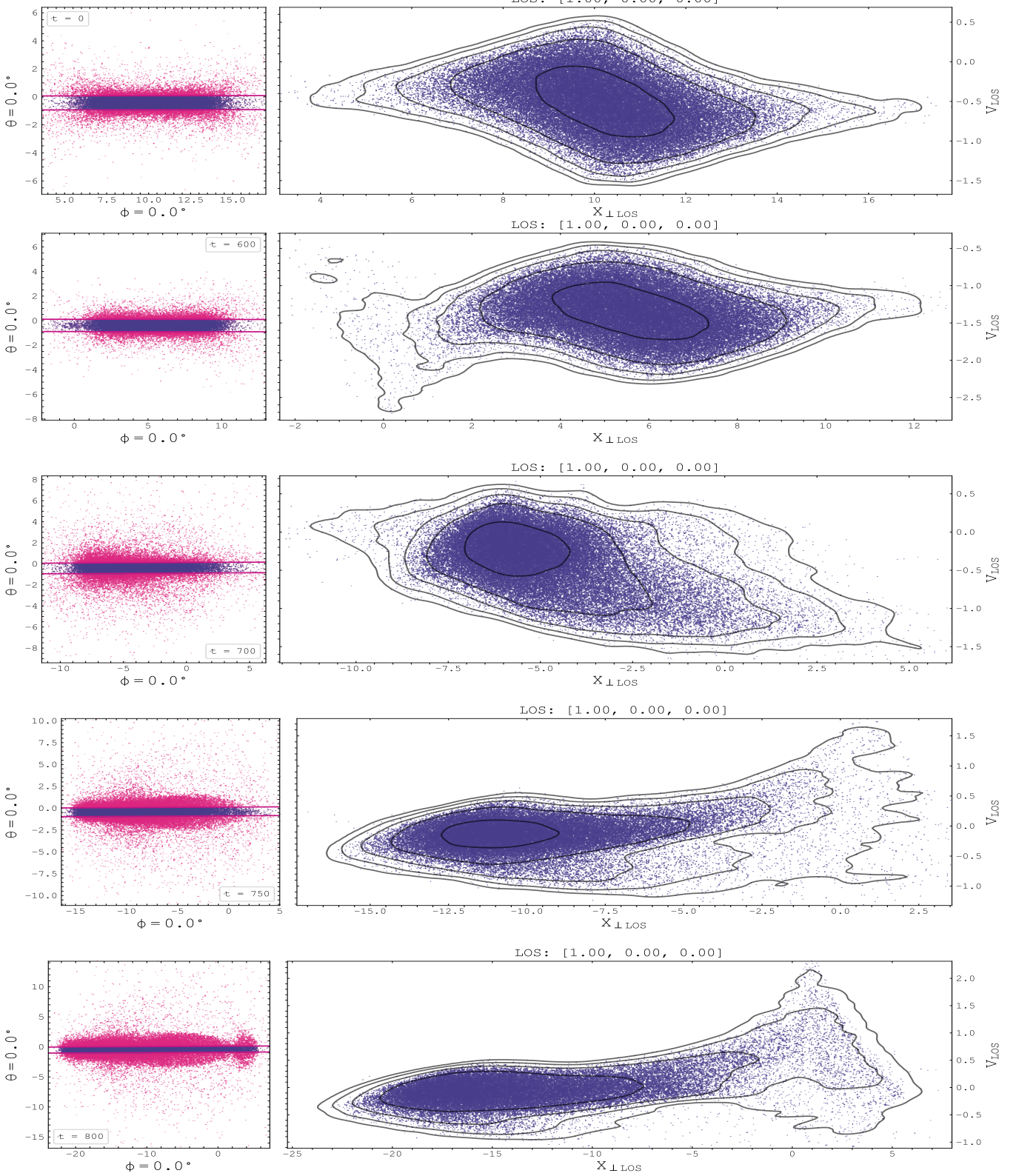


Figure 24. Position–velocity diagram evolution of the third simulation along the \hat{x} line of sight.

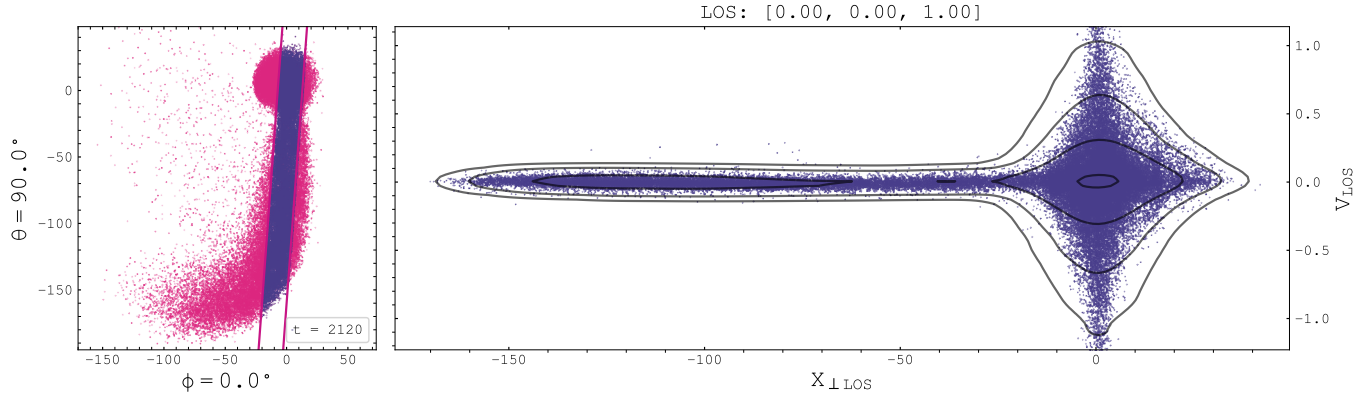


Figure 25. Position velocity diagram of the third simulation along the \hat{z} line-of-sight.